IEEE Open Journal of
Antennas and Propagation

Received 26 March 2022; revised 22 April 2022; accepted 23 April 2022. Date of publication 27 April 2022; date of current version 5 May 2022.

Digital Object Identifier 10.1109/OJAP.2022.3170790

Unique-Solution Single-Sample Complex Dielectric Characterization Through Linear Phase Approximation

CONSTANT M. A. NIAMIEN (Member, IEEE)

Research Institute of Embedded Electronic Systems, Normandie Univ, UNIROUEN, ESIGELEC, IRSEEM, 76000 Rouen, France

CORRESPONDING AUTHOR: C. M. A. NIAMIEN (e-mail: constant.niamien@esigelec.fr)

This work was supported in part by the Project SURFAS, an Interreg France (Channel) England Cross-Border Cooperation Project and in part by the European Regional Development Fund.

ABSTRACT This paper presents a transmission-only (TO) approach that solves the long-standing problem of transmission phase ambiguity. The approach considers a linear frequency-dependent phase approximation to derive the phase mode value analytically and uniquely based on three parameters: the first phase jump frequency, the start frequency, and the start phase value. This formulation leads to a unique propagation constant, easy-to-compute for low-band and wideband applications. In addition, the approach presents a non-iterative loss extraction method based on analytical formulation and curve-fitting. Beyond, the approach corrects standing waves' effect, making it suitable for matched and mismatched lines without any initial guess of the material properties. Numerical and experimental validations confirm the proposed approach for weakly and highly dispersive microstrip samples, including low- and high-loss dielectrics.

INDEX TERMS Dielectric constant, dielectric losses, transmission line measurements.

I. INTRODUCTION

MATERIAL characterization has been of interest for several decades since commonly-used microwave devices, such as antennas, filters, couplers, and power dividers, integrate dielectric and magnetic materials to synthesize the desired functionalities: size-reduction, resonance control, bandwidth increase, etc.

Most material characterization approaches, namely transmission-reflection (TR) and transmission-only (TO) approaches, demand measuring the material sample's S-parameters using dedicated structures like waveguides, coaxial, microstrip lines, etc. Indeed, TR approaches consider the reflection and transmission coefficients [1]–[3], while (TO) approaches focus on the transmission coefficient [4]–[8]. The first limitation with TR approaches is undesired ripples on the extracted material properties every half wavelength due to an ill-behaving term linked to the reflection coefficient's phase. The main techniques that tackle this problem include the nonlinear least-squares approach [2] and the amplitude-only formulation [3]. However, these approaches are iterative, bandwidth-limited, and suggest an initial guess of the material properties or a dedicated constant value.

The second limitation with TR approaches is the same as TO approaches and concerns the transmission coefficient's phase ambiguity, which yields multiple solutions for the extracted propagation constant. However, some relevant methods overcome this limitation, like [4] comparing the measured and calculated group delays to choose the best solution. Other methods consider two samples with different lengths [5] and thicknesses [6] to find the propagation constant's solution. Moreover, the ABCD-matrix formulation addresses the issue with a single 50Ω-matched sample, as proposed in [7]. However, these methods can yield inaccurate results due to fabrication tolerances and standing waves' effect in mismatched lines.

Finally, the Kramers-Kronig approach computes the propagation constant uniquely, knowing the attenuation coefficient [8]. Unfortunately, this helps choose the correct phase mode value but does not provide the propagation constant accurately due to significant errors at the band edges,

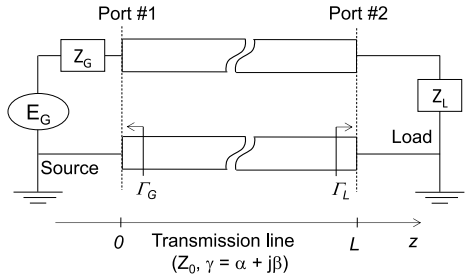

FIGURE 1. Overview of the general measurement system.

obvious for low-band applications. Another limitation is the broadband requirement for the attenuation coefficient.

In sum, most existing approaches do not solve the transmission coefficient's phase ambiguity problem for arbitrary bandwidths and line impedances without any initial guess of the material properties and a built-in constant.

This paper presents a TO approach that solves this long-standing problem by deriving a general analytical formula for the phase mode value based on a linear frequency-dependent phase approximation. The approach then formulates a unique propagation constant suitable for any frequency band and impedance matching level, considering a single material sample. Compared with most relevant approaches, the present approach is:

i) simple, non-iterative, and easy to compute with standard post-processing software, knowing the complex transmission coefficient,
ii) suitable for arbitrary lines, including both 50Ω-matched and mismatched lines, such as microstrip and coplanar waveguide types,
iii) guess-free since it does not require any initial input data other than the needed transmission coefficient,
iv) bandwidth-independent since it includes both low and wideband options.

The proposed approach is validated numerically and experimentally, considering weakly and highly dispersive dielectrics. Validation includes microstrip samples, preferred over coplanar ones for their geometrical simplicity and extensive analytical formulations [9]–[16].

This paper is organized as follows. Section II reviews the transmission coefficient's phase issue and formulates the present approach's solution. In addition, Section III details the extraction methodology of the complex permittivity validated in Section IV with full-wave simulations. Validation includes different permittivity, loss, dispersion, and impedance matching levels. Finally, Section V compares the present approach with experiments over various samples.

II. FORMULATION

A. REVIEW OF THE PROBLEM

Let us consider a general two-port transmission line, loaded at port #1 by a radio-frequency (RF) source, and at port #2, by a load, Z_L, as depicted in Fig. 1.

The transmission line (microstrip, coplanar, etc.) supports a transverse electromagnetic mode (TEM) whose complex propagation constant is denoted by $\gamma = \alpha + j\beta$, α represents the attenuation coefficient, while β is the intrinsic propagation constant.

For a general wave propagation scenario where the line's characteristic impedance (Z_0) differs from the source and load impedances, reflections occur at the line's input and end with reflection coefficients Γ_G and Γ_L, respectively, seen from the line. Therefore, based on a multiple-reflection viewpoint [17, p. 74] and invoking some mathematical relationships with geometric series, one can derive the transmission coefficient between ports #2 and #1 as:

$$S_{21} = e^{-\gamma L} \tag{1}$$

The simple form of (1), only dependent on γ and L, indicates that the successive reflections do not affect the transmission coefficient (S_{21}). However, in practice, as seen in Section IV, little reflections are still present on S_{21} as small ripples, increasing with the mismatching level.

From (1), it is straightforward to derive α and β as:

$$\alpha = -\frac{\ln|S_{21}|}{L} \tag{2a}$$

$$\beta = -\frac{\theta_{21} - 2\pi m}{L} \tag{2b}$$

where θ_{21} represents the unwrapped phase of S_{21}, L is the line length, and m is a positive integer denoting the phase mode.

Equation (2a) – (2b) obtained here for a general two-port transmission line is similar to [8, eqs. (7) and (8)], considering a material sample placed in a waveguide structure.

From (2a), it is straightforward to get α knowing $|S_{21}|$ and L. However, (2b) has two unknowns (β, m) for a single equation at hand, which leads to infinite solutions mathematically.

The following section addresses this well-known problem of solution ambiguity [1]–[8].

B. FORMULATION

From the general RLCG circuit model [17, pp. 49–51], the complex propagation constant of a lossy transmission line can be written as:

$$\gamma = \alpha + j\beta = jk_0\sqrt{\left(\varepsilon_e' - j\varepsilon_e''\right)\left(\mu_e' - \mu_e''\right)} \tag{3}$$

where $\varepsilon_e = \varepsilon_e' - j\varepsilon_e'' = C/C_0 - -jG/L_0\omega$ is the effective permittivity, $\mu_e = \mu_e' - j\mu_e'' = L/L_0 - jR/L_0\omega$ is the effective permeability, $k_0 = \omega/c$ is the free space wavenumber, ω denotes the angular frequency, and c, the light speed in free space. Parameters R, L, C, and G represent the per-unit length series resistance, series inductance, shunt capacitance, and shunt conductance. However, L_0 and C_0 denote the corresponding inductance and capacitance of the same line filled with air. Generally, L splits as the sum of the internal and external

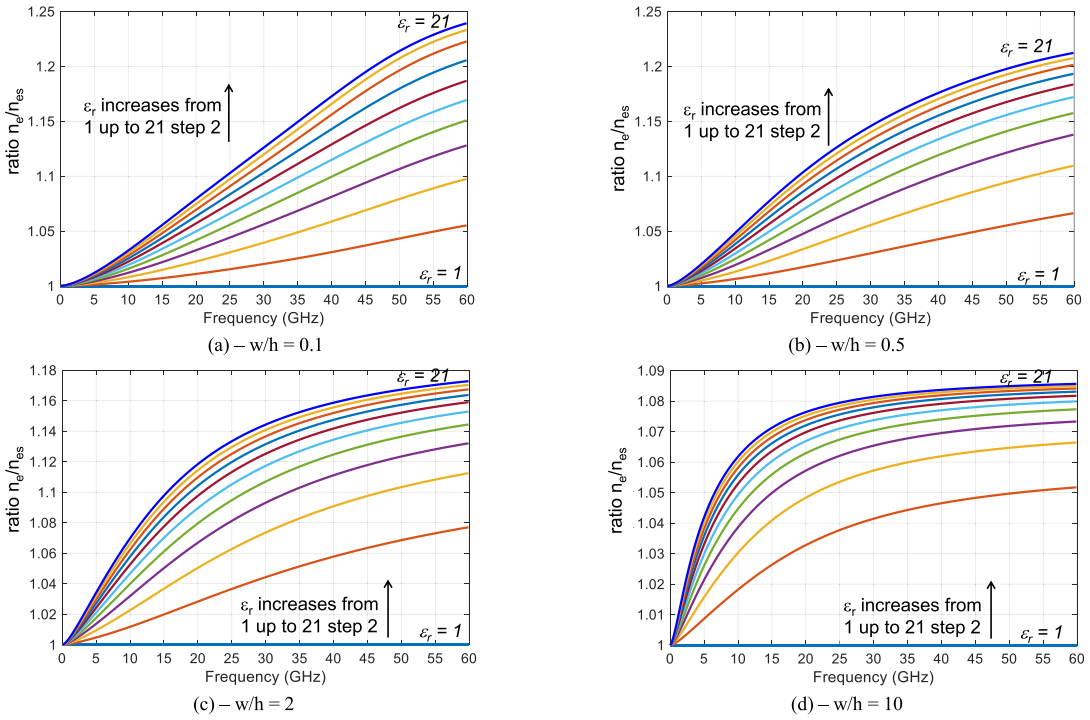

FIGURE 2. Frequency dispersion of the microstrip line's effective refractive index (n_e) normalized by its static value (n_{es}), based on Kirschning and Jansen's model [9]. The static index (n_{es}) is obtained from [14].

inductances, $L = L_{int} + L_{ext}$, where $L_{ext} = L_0$ is frequency independent, linked to the magnetic field distribution inside the surrounding air region. However, L_{int} is frequency-dependent, related to the magnetic field distribution inside the conductor (skin depth) and the material beneath the conductor [7].

Knowing γ through (α, β) is not sufficient to determine the four unknown material parameters (ε_e', ε_e'', μ_e', μ_e'') using only one equation. Therefore, the following assumptions are considered.

1) ASSUMPTIONS

1) The material of interest is purely dielectric with a relative permittivity of ε_r and loss tangent of $tan\delta$, excluding pure magnetic or magneto-dielectric materials. This simplification is not limiting in practice since many standard microwave devices (antennas, filters, etc.) are based on dielectric materials,
2) The material loss is such that $\varepsilon_e''\mu_e'' << \varepsilon_e'\mu_e'$, which covers low-loss dielectrics (low ε_e'') with high or relatively poor conductivity lines (high μ_e'') and high-loss dielectrics (high ε_e'') with relatively high conductivity lines (low μ_e''),
3) The internal inductance (L_{int}) is negligible compared with the external inductance (L_{ext}), that is, $L_{int}/L_{ext} << 1$, leading to $\mu_e' = 1 + L_{int}/L_{ext} \approx 1$. This assumption is valid for dielectrics, assumed in *i)*.

The following key relationships are derived based on the above assumptions and according to (3) as:

$$\frac{\beta^2 - \alpha^2}{k_0^2} = \varepsilon_e'\mu_e' - \varepsilon_e''\mu_e'' \approx \varepsilon_e' \tag{4a}$$

$$\frac{2\alpha\beta}{k_0^2} = \varepsilon_e''\mu_e' + \varepsilon_e'\mu_e'' \approx \varepsilon_e'' + \varepsilon_e'\mu_e'' \tag{4b}$$

It is evident from (4a) that knowing α and β provides ε_e'. However, knowing α, β, and ε_e' is not sufficient to get the dielectric loss ε_e'' from (4b) since the conductor loss linked to $\mu_e'' = R/L_{ext}\omega$ is unknown. Indeed, (4b) involves the sum of two terms related to the dielectric and conductor losses in the line. As a result, the conductor loss becomes negligible for high-conductivity lines, leading (4b) to give ε_e'' approximately. However, the dielectric and conductor losses must be determined separately in a more general approach. Section III-B details the proposed approach.

2) UNIQUE SOLUTION FOR β

Replacing β in (2b) by the guided propagation constant k_g allows deriving the unwrapped phase θ_{21}. That is:

$$\theta_{21} = -\frac{2\pi f n_e L}{c} + 2\pi m \tag{5}$$

where $k_g = k_0 n_e$, $n_e = \sqrt{\varepsilon_e'}$ is the effective refractive index, and f denotes the frequency.

As seen from (5), the frequency dependence of θ_{21} is from the product fn_e. For most dielectric materials, although ε_e' may vary significantly with frequency, n_e only changes slowly compared to its static value n_{es}. Figs. 2a – 2d confirms

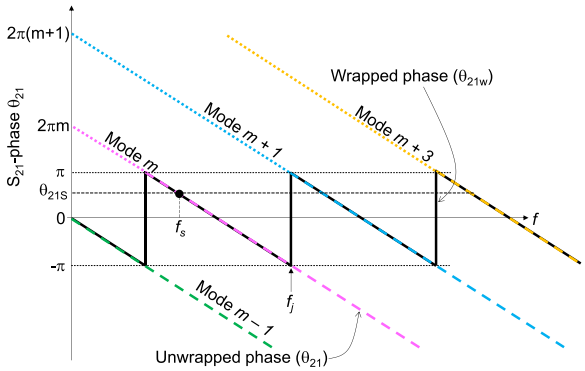

FIGURE 3. S_{21}-phase mode analysis with frequency *f*.

this behavior from the plots of the ratio $n_e(f)/n_{es}$ from DC to 60 GHz for different permittivity ε_r ranging from 1 up to 21. Computations are based on Kirschning and Jansen's dispersion model [9], which features accuracy better than 0.6% for $0.1 \le W/h \le 100$ and $1 \le \varepsilon_r \le 20$.

Indeed, Figs. 2a – 2d shows that n_e/n_{es} only varies between 1 and 1.25 for $W/h \le 1$ and $W/h \ge 1$ regardless of frequency. Consequentially, the following key assumptions are made:

$$\frac{dn_e}{df} \approx 0 \tag{6a}$$

$$n_e(f) \approx n_e(0) = n_{es} \tag{6b}$$

Therefore, from (6a) – (6b), (5) may be rewritten as:

$$\theta_{21} \approx -Kf + 2\pi m \tag{7}$$

where $K = 2\pi n_{es}L/c$ is a constant depending on the static refractive index (n_{es}) and the sample length (L).

Equation (7) indicates that the unwrapped phase of the transmission coefficient θ_{21} almost linearly varies with frequency regardless of the material properties. This result is the basis of the present approach, indicating that two points (f, θ_{21}) are sufficient to determine m uniquely.

Let us plot θ_{21}(f) for an arbitrary K value, as depicted in Fig. 3, also showing the wrapped phase θ_{21w}.

As seen in Fig. 3, θ_{21} and θ_{21w} coincide from the start frequency (f_s) until θ_{21w} jumps for the first time from $-\pi$ to π, typically at frequency f_j. Consequentially, with the two characteristic points (f_s, θ_{21s}) and (f_j, $-\pi$), one can get m uniquely based on (7), as:

$$m = int\left(\frac{f_s\pi + f_j\theta_{21s}}{2\pi\left(f_j - f_s\right)}\right) \tag{8}$$

where function *int(x)* means taking the integer part of x.

Analysis of (8) and Fig. 3 indicates that the user directly sets m by choosing f_s for a given material of interest. However, m also includes the material effect through the start phase value $\theta_{21s} = \theta_{21w}(f_s) = \theta_{21}(f_s)$. In practice, the user must choose f_s not close to f_j to avoid a numerical singularity due to the difference $(f_j - f_s)$ in the denominator. Beyond that, it is worth mentioning that (8) solves the long-standing ambiguity problem in finding m precisely. Near DC-frequency, (8) leads to $m \approx int(\theta_{21s}/2\pi) \approx 0$ since $\theta_{21s} \approx 0$. Therefore, the zero-phase mode value can be anticipated for applications starting near the DC frequency, as in [7]. However, the phase mode value will not necessarily be zero as the start frequency increases. It will depend on the start frequency (f_s) and the material properties, setting f_j and θ_{21s}.

Invoking (8) in (2b) provides a unique solution for β knowing θ_{21} and L.

Validity of (8) covers dispersive dielectric materials in microstrip line technology. This includes other line technologies such as coplanar waveguide (CPW) lines with thin thicknesses (less dispersive), typically verifying $n_{es} > n_{e0} = 2\sqrt{\varepsilon_r}/(3 + g(f_{TE}/f)^{1.8})$, where the cutoff frequency for the first surface wave TE_0-mode is $f_{TE} = c/(4h\sqrt{(\varepsilon_r - 1)})$, and the geometrical parameter g is defined in [18, p. 413]. Other CPW lines with a backing conductor or finite ground planes are also included since they are less dispersive and show a dispersion behavior comparable to a microstrip line [18, p. 413]. Beyond these two standard transmission lines (microstrip, CPW), one can include other line technologies as long as (1) and (6a) – (6b) are valid.

Now that m and β are determined uniquely, the complex permittivity $\varepsilon_e = \varepsilon'_e - j\varepsilon''_e$ can be extracted.

III. COMPLEX PERMITTIVITY EXTRACTION

A. PERMITTIVITY EXTRACTION

The permittivity extraction method starts by choosing the operating bandwidth $[f_s, f_{stop}]$, the transmission line (sample) length (L), and the number of frequency points (N) or the step size (Δf). These initial sets precede measuring or simulating the two-port sample's S_{21-} parameter. Fig. 4 presents the flowchart of the extraction method.

Step #1: Following the prerequisites, the user must invoke (8) to calculate the S_{21}-phase mode value m.

Step #2: The intrinsic propagation constant β is derived from (2b) based on m, the attenuation coefficient α obtained from (2a), and the unwrapped phase θ_{21} derived from the raw S_{21}-phase (wrapped phase θ_{21w}).

Step #3: Invoking now (4a) allows calculating ε'_e from which surface waves' effects must be removed using Kirschning and Jansen's dispersion model [9] to get ε_{re}, the effective permittivity without surface waves' effects. In [7], ε_{re} refers to the "apparent" effective permittivity carrying conductors' effect with $1/\sqrt{f}$-behavior. The present approach neglects this effect, as mentioned in Section II-B1. Finally, the relative permittivity ε_r is derived from ε_{re} based on Hammerstad's formula [14]. Performing this last calculation jointly with the previous one involving the dispersion model is mandatory since both computations are inter-dependent through ε_r, embedded in function P reported in [9].

B. LOSS TANGENT EXTRACTION

As mentioned in Section II-B, (4b) does not provide ε''_e directly since μ''_e is unknown, linked to the external

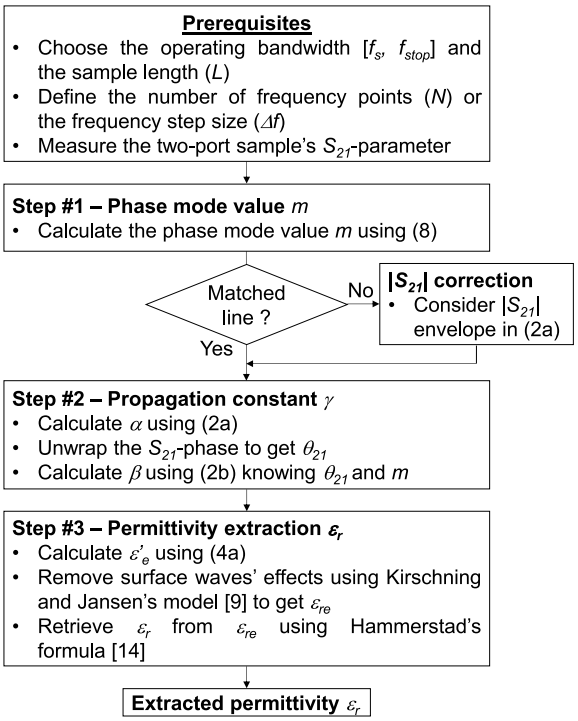

FIGURE 4. Flowchart of the permittivity extraction method.

inductance (L_{ext}) and the series resistance (R) of the line. Besides, one can note that the attenuation coefficient α splits into two terms: the effective dielectric and conductor losses, α_{de} and α_{ce}, respectively. Moreover, as reported in [18, pp. 102–108] and [7], α_{de} varies the same as $f\sqrt{\varepsilon'_e}$, while α_{ce} follows $\varepsilon'_e\sqrt{f}$. Based on these results and making use of Kirschning and Jansen's dispersion model applied here to the effective loss tangent ($tan\delta_e$), the dielectric loss tangent ($tan\delta$) can be extracted as:

$$\alpha = \underbrace{a_0\sqrt{\varepsilon'_e}f}_{\alpha_{de}:dielectric\ \ loss} + \underbrace{b_0\varepsilon'_e\sqrt{f}}_{\alpha_{ce}:conductor\ \ loss} \tag{9a}$$

$$\tan\delta_e = \frac{a_0 c}{\pi} \tag{9b}$$

$$\tan\delta = \frac{P}{1+P}\tan\delta_e + \frac{1}{1+P}\tan\delta_{es} \tag{9c}$$

where $tan\delta_{es}$ is the static effective loss tangent, function P is defined in [9], parameters a_0 and b_0 are frequency-dependent and may be obtained by a least-square fitting method. Knowing b_0 may provide the conductors' conductivity from its analytical expression reported in [18, p.108].

It is worth mentioning that (9a) – (9c) is valid for low-loss dielectrics, typically for $tan\delta < 0.1$. However, for high-loss dielectrics verifying $tan\delta \geq 0.1$, one may consider the following formula [18, p. 108]:

$$\tan\delta = \frac{\lambda_0\alpha_{de}}{3.143}\frac{\varepsilon_r - 1}{\varepsilon_r}\frac{\sqrt{\varepsilon_{re}}}{\varepsilon_{re} - 1} \tag{10}$$

where $\alpha_{de} \approx \alpha$, indicating that the dielectric loss predominates over the conductor loss, assumed negligible.

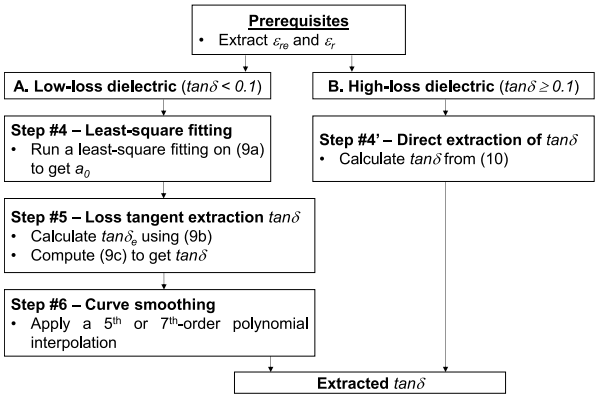

FIGURE 5. Flowchart of the loss tangent extraction method.

Therefore (10) is suitable for high-loss dielectrics with high-conductivity lines, while (9a) – (9c) fits low-loss dielectrics with high or relatively poor conductivity lines.

Fig. 5 presents the flowchart of the loss tangent extraction method, including two paths whose prerequisites are the extracted permittivities ε_{re} and ε_r.

Indeed, path A is suitable for low-loss dielectrics while splitting dielectric and conductor attenuation coefficients based on a standard least-square fitting approach, providing a_0 (Step #4). The loss tangent is then derived using (9c) from (9b), giving $tan\delta_e$ (Step #5). The value of the static effective loss tangent $tan\delta_{es}$ reported in (9c) is simply the low-frequency value of $tan\delta_e$, ideally at DC-frequency. Setting $tan\delta_{es}$ below one or two GHz may be accurate enough in practice.

In addition, it is essential to note that the loss curve fitting of (9a) is a banded process, starting with an initial low bandwidth (of about 50 MHz) to increase accuracy, followed by several broader bandwidths (of about 5 GHz), providing a good tradeoff between accuracy and fitting error suppression. Indeed, except for the initial band, low bandwidths may lead to wrong fittings, tracking the curve's insignificant details instead of its overall profile. Therefore, the following sections assume the above fitting presets.

Finally, since this banded fitting process leads to a stairs-like function, the resulting loss function $tan\delta$ is smoothed using a conventional fifth or seventh order polynomial interpolation (Step #6).

Path B fits high-loss dielectrics with negligible conductor loss. In this case, (10) directly gives $tan\delta$ (Step #4').

C. STANDING WAVES' EFFECT CORRECTION

Impedance mismatching between the transmission line (sample) and the RF source or the load creates successive reflections that sum as standing waves, whose amplitudes increase with the mismatching. Even though these waves do not appear in (1), they affect the measured or simulated S_{21} as small ripples, overlaying the theoretical S_{21}. Full-wave simulations show that the standing waves, which start from about $S_{ii} > -20$ dB, are more assertive on the S_{21}-amplitude

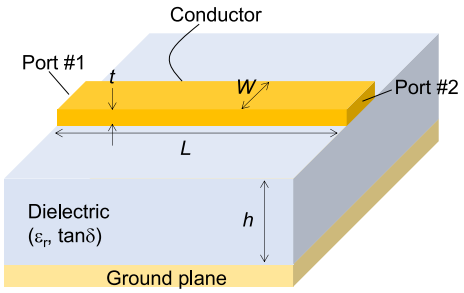

FIGURE 6. The two-port microstrip line sample.

TABLE 1. Dimensions of the microstrip line samples.

Parameter	L	W	h
Unit : mm	90	1.55	0.8

than the phase θ_{21}. Therefore, from a simplified viewpoint, the measured or simulated S_{21} may be viewed as a transmission coefficient, amplitude-modulated by the theoretical S_{21}. Consequently, it is convenient to extract the "correct" S_{21}-amplitude by taking the envelope of the measured or simulated S_{21}. This correction applies to mismatched lines before Step #2, as mentioned in Fig. 4.

The following section compares the proposed approach with full-wave simulations.

IV. NUMERICAL VALIDATIONS

Let us focus now on a microstrip-type transmission line to compare the proposed approach with full-wave simulations. Following the same approach with the appropriate theoretical formulas, other transmission line types, such as coplanar waveguides, may also be considered.

Fig. 6 presents the two-port microstrip line sample, including its geometrical parameters: length L, width W, height h, and conductor thickness t. All conductors are set to perfect electric conductors (PEC) to simplify the simulation model with $t = 0$. Table 1 gives the samples' dimensions.

The microstrip line is printed on three different materials following the exact dimensions, typically FR4-like $4.3(1 - j0.025)$ and AD1000-like $10.2(1 - j0.0023)$, representing weakly dispersive low-loss dielectrics. The third material is ECCOSORB LS-20 [19], a highly dispersive high-loss dielectric with $2.32(1 - j0.\ 93)$ around 2 GHz.

Each sample is fed at port #1 by a 50Ω-source and 50Ω-loaded at port #2. The structure is designed and simulated with CST, based on the Finite Integration Technique [20]. On the one hand, simulations provide the two-port S-parameters needed to compute the proposed approach, while on the other hand, they directly provide the intrinsic propagation constant β. Finally, for comparison needs, the Kramers-Kronig approach is also computed from the attenuation coefficient (2a), as [21]:

$$\beta_{K-K} = k_0 + k_0 \frac{2c}{\pi} P_K \int_{\omega_s}^{\omega_{stop}} \frac{\alpha(\omega')}{\omega'} \frac{d\omega'}{|\omega' - \omega|} \qquad (11)$$

TABLE 2. Values of the s21-phase mode m and P_K for different operating bandwidths and materials.

Bandwidth (GHz)	#1 [0.010, 20]	#2 [2, 20]	#3 [4, 8]
FR4-like	$m = 0$ $P_K = 5$	$m = 1$ $P_K = 5$	$m = 2$ $P_K = 5$
AD1000-like	$m = 0$ $P_K = 55$	$m = 2$ $P_K = 55$	$m = 3$ $P_K = 60$
ECCOSORB LS	$m = 0$ $P_K = 0.1$	$m = 1$ $P_K = 0.1$	$m = 2$ $P_K = 0.1$

m values are obtained from (8), while P_K is set empirically.

where $\omega_s = 2\pi f_s$, $\omega_{stop} = 2\pi f_{stop}$, while parameter P_K corrects the integral value for a finite bandwidth integration instead of an infinite bandwidth, as defined in [21]. This parameter refers to the integral's "principle value" in [8].

Table 2 gives the corresponding P_K and m values for the different materials for three operating bandwidths $[f_s, f_{stop}]$. Since there is no general rule for adjusting P_K, it is set empirically.

In what follows, β is computed from the proposed approach and compared with Kramers-Konig and FIT for the three dielectrics. The considered bandwidths are [0.010, 20], [2], [20], and [4], [8], all in GHz.

A. WEAKLY DISPERSIVE LOW-LOSS DIELECTRICS

1) CASE OF A 50Ω-MATCHED LINE

As seen in Fig. 7a, the FR4-like sample corresponds to a matched line, showing a reflection coefficient $S_{ii} < -20$ dB at ports #1 and #2. The absence of ripples on S_{21} and α confirms this result, as seen in Figs. 7b and 7c, respectively. Beyond that, Fig. 7c indicates that the extracted conductor loss (α_{ce}) is negligible compared with dielectric loss (α_{de}), almost equal to the total loss (α). This result complies with the physics since conductors are set to PEC in simulation, which prevents any ohmic loss with infinite conductivity.

Figs. 7d – 7f presents the extracted β for the three bandwidths. It is seen that the proposed approach correlates with the FIT for all three bandwidths. However, the Kramers-Kronig approach shows significant errors in low bandwidths, corresponding to an overall curved profile with drops at the band boundaries. Another limitation is the precise adjustment of P_K, requiring a reference β, which suggests anticipating the material properties. On the other hand, accuracy improves as bandwidth increases, particularly true on the lower edge (Fig. 7f).

Inaccuracy in the Kramers-Kronig formulation (11) is mainly due to the loss of information on the attenuation coefficient (α), shrunk to the bandwidth of interest instead of an ideally infinite bandwidth [21]. In contrast, the proposed approach does not invoke a "truncated" integration since α and β are entirely determined separately and uniquely from S_{21}, providing m from a simple computation.

2) CASE OF A MISMATCHED LINE

The AD1000 microstrip sample is not 50Ω-matched, as noted from Fig. 8a, showing the reflection coefficients S_{11} and S_{22}, which increase up to −7 dB. As a result, ripples

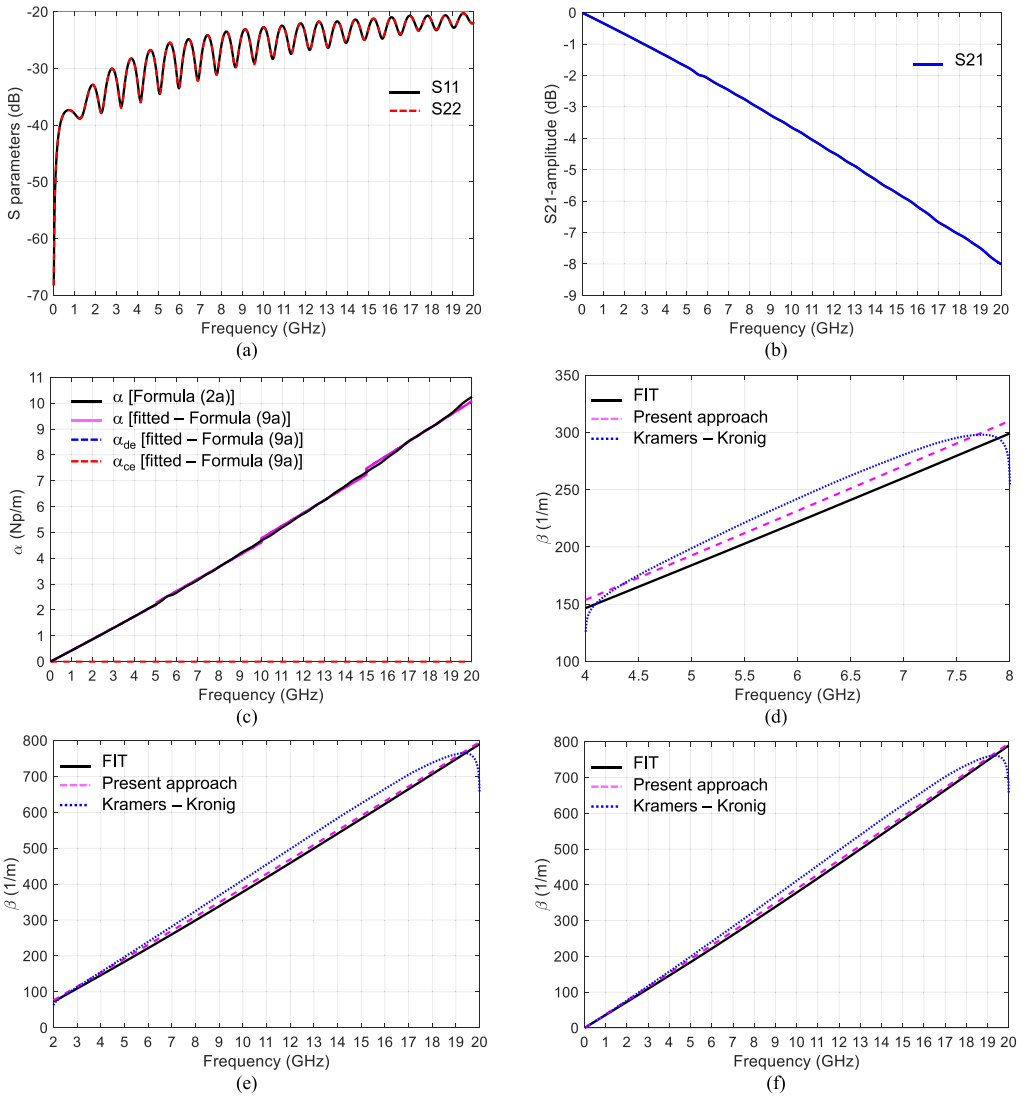

FIGURE 7. The FR4-like microstrip sample, (a): simulated reflection coefficients S_{11} and S_{22}, (b): simulated transmission coefficient S_{21}, (c): extracted attenuation coefficient α, (d) – (f): extracted propagation constant β over the bandwidths (in GHz) of [4], [8], [2], [20], and [0.010, 20], respectively.

occur on S_{21}, as depicted in Fig. 8b. The reduced characteristic impedance to $Z_0 \approx 33\Omega$, following the permittivity increase from 4.3 for the FR4-like sample to 10.2, explains this impedance mismatching.

Correcting the ripples in S_{21}, according to Fig. 4, provides α from which dielectric and conductor losses are extracted based on (9a). Similar to Fig. 7c, Fig. 8c confirms that dielectric loss predominates over conductor loss, which is negligible due to PEC conductors.

The extracted β in Figs. 8d – 8f confirms that the proposed approach correlates with the FIT even for a mismatched microstrip line. Besides, the Kramers-Kronig approach remains inaccurate for low bandwidths and improves as bandwidth increases.

Figs. 9a and 9b present the extracted permittivity ε_r and loss tangent $tan\delta$ of the FR4-like and AD1000-like materials, respectively, based on the methods in Figs. 4 and 5. The extracted properties are compared with the input data considered in the simulation.

Figs. 9a and 9b show that the extracted ε_r and $tan\delta$ correlate well with the input data for the two materials. In addition, the permittivity error is smaller than 0.08% and 0.6% for the FR4-like and AD1000-like samples, respectively. However, the permittivity error rises at low frequency for three reasons: *i)* the line length becomes electrically short, *ii)* the line's internal inductance becomes non-negligible as it increases with a $1/\sqrt{f}$-factor as frequency decreases, and *iii)* errors from the analytical formulas for the static and dispersive permittivities, ε_{res} [14] and ε_{re} [9], increase at low frequencies, as seen in Figs. 10a – 10c. Indeed, Figs. 10a – 10c show that analytical values of ε_{re} are slightly overestimated compared with full-wave simulations at low frequencies, contributing to slightly higher extracted $\varepsilon_r(|\Delta\varepsilon_{re}| < 0.5)$, as seen in Fig. 9a.

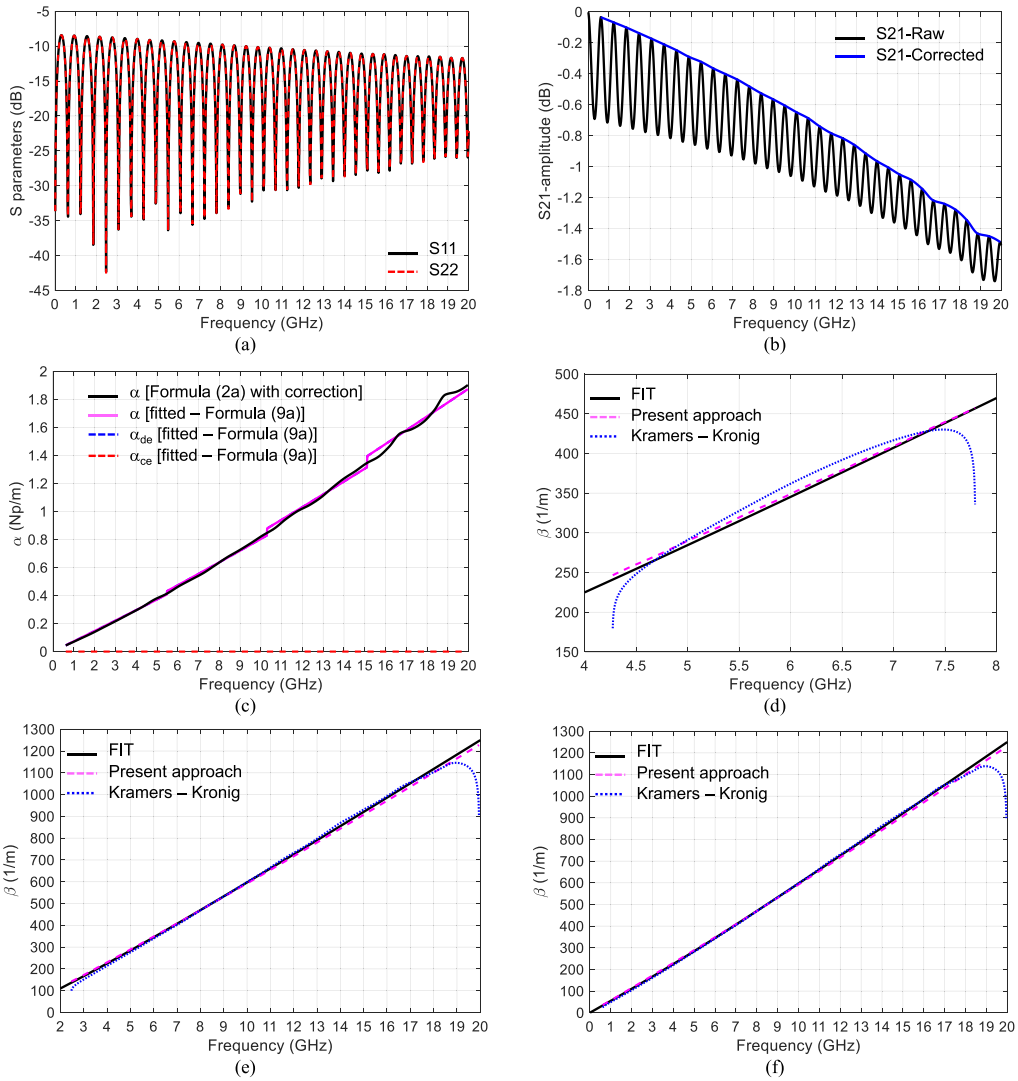

FIGURE 8. The AD1000-like microstrip sample, (a): simulated reflection coefficients S_{11} and S_{22}, (b): simulated transmission coefficient S_{21}, (c): extracted attenuation coefficient α, (d) – (f): extracted propagation constant β over the bandwidths (in GHz) of [4], [8], [2], [20], and [0.010, 20], respectively.

Beyond that, standing waves with the AD1000-like sample explain the slight oscillations on ε_r and higher error than the FR4-like sample, particularly at low frequencies below 1 GHz.

Overall, the permittivity error for both samples is weak and stands below 0.6% over the entire band up to 20 GHz.

Regarding loss tangent, the relative error over the entire frequency band up to 20 GHz is smaller than 0.00278 and 0.00032 for the FR4-like and AD1000-like samples, respectively. Therefore, these error ranges are acceptable since they are nearly ten times smaller than the loss tangent values.

In sum, choosing the sample length sufficiently long, typically such that $L \geq 0.3\lambda$, helps maintain these orders of accuracy by decreasing the error in ε_r at low frequencies. Moreover, in practice, relatively long samples ($L \geq 0.3\lambda$) help measure low-loss materials over low frequencies accurately by increasing the S_{21} level, which may be low and challenging to acquire precisely depending on the measurement sensitivity.

B. HIGHLY DISPERSIVE HIGH-LOSS DIELECTRIC

This dielectric case with high loss and strong frequency dispersion is implemented with the ECCOSORB LS-20 material [19]. This product is an RF absorbing material used for antenna isolation and Q-factor lowering in cavity-based devices such as RF amplifiers, oscillators, etc.

The ECCOSORB LS-20 microstrip sample is simulated with CST based on the microstrip line's dimensions in Table 1. Figs. 11a – 11d presents the simulated and extracted properties according to the methods detailed in Figs. 4 and 5 (path #B).

Fig. 11a shows the reflection coefficients at ports #1 and #2, along with the transmission coefficient S_{21}, which decreases to -36 dB at 20 GHz, indicating high dielectric loss (without conductor loss). Fig. 11b plots the attenuation coefficient α, confirming high loss.

The extracted β, depicted in Fig. 11c, still fits the FIT, while the Kramers-Kronig's accuracy remains poor at the band's upper edges.

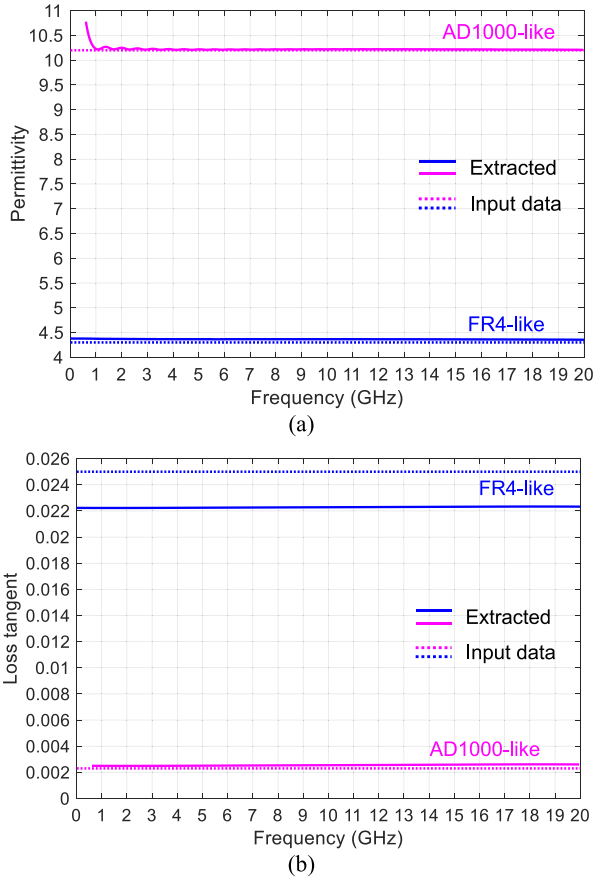

FIGURE 9. The extracted properties of the FR4-like and AD1000-like microstrip samples, (a): permittivity ε_r, (b): loss tangent $tan\delta$.

The extracted properties (ε_r, $tan\delta$) correlate with the simulation properties, referred to as input data in Fig. 11d. It is seen that the permittivity rapidly decreases from 7 to 2.3 within 10 MHz – 2 GHz, while the loss tangent rapidly grows to 0.9 at 2 GHz and then decreases to 0.27 at 20 GHz. Despite these substantial variations, the error bound on ε_r remains smaller than 11%, while the relative error on $tan\delta$ is below 0.08. Therefore, these error bounds are acceptable.

Most of the differences on ε_r occur below 1 GHz, explained by the typical low-frequency issues mentioned previously, related to the analytical formulas' errors, the sample length, and the internal inductance effects. However, the minor differences in $tan\delta$ may be attributed to numerical inaccuracies in modeling and meshing a highly dispersive material.

Following this numerical validation, the following section focuses on experiments.

V. EXPERIMENTS

A. SAMPLES

Experiments consider three standard materials commonly used in antenna and RF component/circuit designs, typically FR4 ($\varepsilon_r = 4.2$, $\tan\delta = 0.014$) [22], AD600L ($\varepsilon_r = 6.15$, $\tan\delta = 0.003$) [23], and AD1000 ($\varepsilon_r = 10.2$, $\tan\delta = 0.0023$) [21], specified at 2 and 10 GHz, respectively.

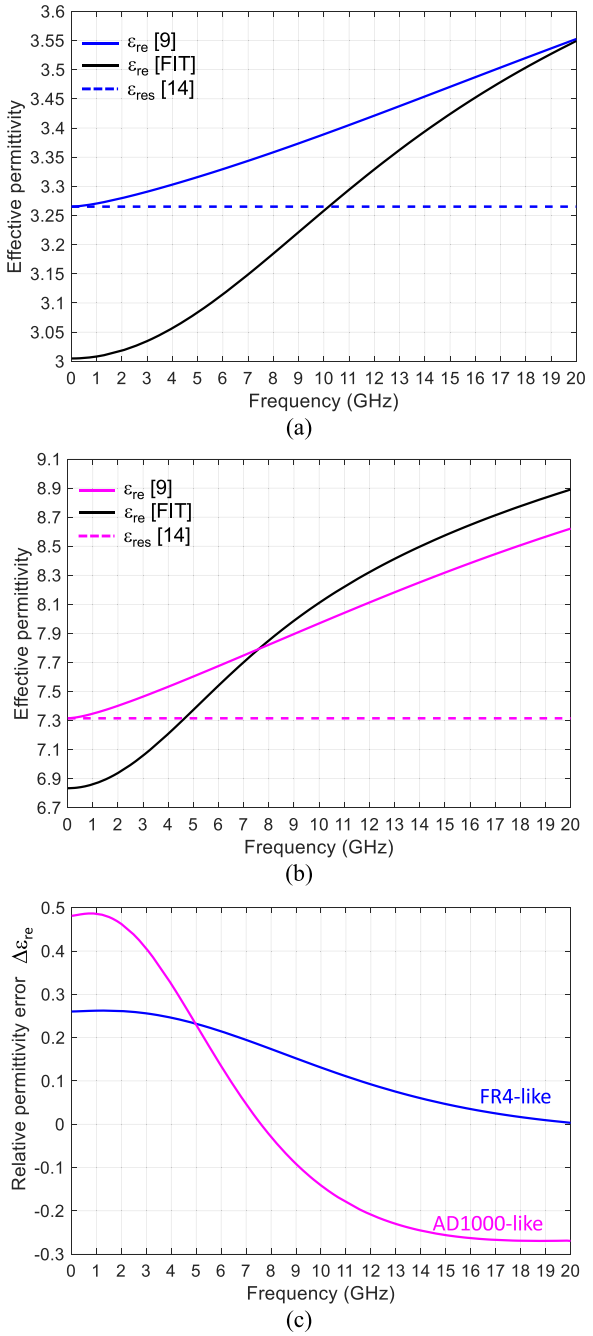

FIGURE 10. The simulated (FIT) and analytical effective permittivities, (a): case of FR4-like, (b): case of AD1000-like, (c): relative error $\Delta\varepsilon_{re}$. The relative error is obtained by $\Delta\varepsilon_{re} = \varepsilon_{re\text{-}analytical} - \varepsilon_{re\text{-}simulation}$, where analytical ε_{re} is obtained from the effective static permittivity (ε_{res}) [14], invoked in the dispersion formula [9].

TABLE 3. Thicknesses of the fabricated microstrip samples.

Material	*FR4*	*AD600L*	*AD1000*
h (mm)	0.787	0.787	0.762

The microstrip samples have the same length of $L = 40$ *mm* and width of $W = 1.55$ *mm*. The ground size is 40 x 100 mm^2.

Three microstrip lines are designed and fabricated on these materials with the same length of $L = 40$ *mm* and width of $W = 1.55$ *mm* but with different thicknesses given in Table 3. Metallization is an 18 μm-thick Copper sheet.

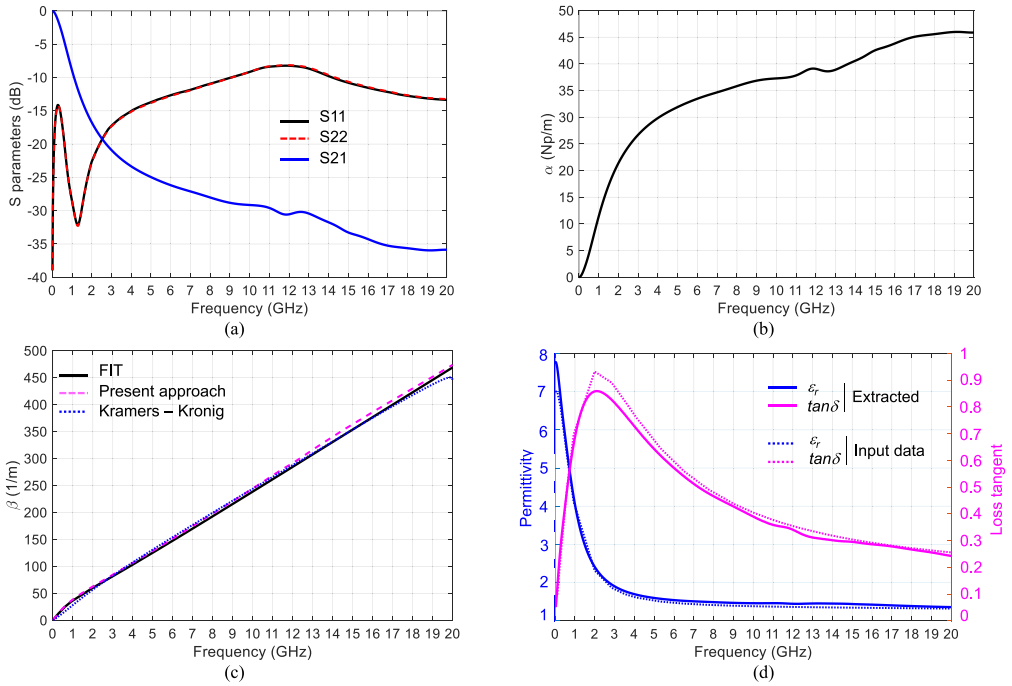

FIGURE 11. The ECCOSORB LS-20 microstrip sample, (a): simulated reflection and transmission coefficients S_{11}, S_{22}, and S_{21}, (b): extracted attenuation coefficient α, (c): extracted propagation constant β, (d): extracted permittivity ε_r and loss tangent $tan\delta$. The S_{21}-phase mode for this frequency band of [0.010, 20] in GHz is $m = 0$, as reported in Table 2.

B. MEASUREMENT SYSTEM

The samples are fabricated and tested based on Figs. 1 and 6, without RF connectors to prevent their parasitic effects. Instead, an RF Test Fixture Model 3680V from ANRITSU [24] is used. This system includes two test ports, one fixed and the other movable, including an air-based coaxial termination with a vertically movable lower jaw to grip the sample's ground plane. At the same time, the upper central pin lands on the sample's feed line.

Fig. 12a presents the general mounting set of a microstrip sample on a single test port, while Fig. 12b zooms on the test port's photograph.

Furthermore, each test port's backside leans on a 1.85 mm-type coaxial connector, connected to the Vector Network Analyzer's port through a standard 1.85 mm-coaxial cable. Fig. 12c presents the AD1000 sample mounted on the two-port RF test fixture.

C. CALIBRATION

The calibration invokes a set of microstrip samples, including five "Through" lines, two "Open" and "Short" lines, and a broadband 50Ω dual-termination. Fig. 13a lists the complete set of the microstrip samples available in the calibration kit Model 36804B-10M, while Fig. 13b presents the samples' photographs.

The Through-Reflect-Match (TRM) calibration [25], also denoted as Line-Reflect-Match (LRM) calibration [24], is preferred over an LRL calibration, also referred to as TRL, to get a wideband calibration with reasonable accuracy [24]. Indeed, the TRM calibration ensures low-frequency accuracy, whereas the TRL calibration is inherently inaccurate, overestimating the extracted loss tangent. In contrast, the TRL calibration is slightly more accurate than the TRM calibration at higher frequencies, but both calibrations provide almost the same accuracy for permittivity extraction.

The implemented two-port TRM calibration invokes a "Through," two "Reflect," and a "Match." The "Reflect" is implemented with a "Short" by simply leaving closed the lower jaw of the test port. The dual-50Ω-termination implements the "Match," while each microstrip line sample in the kit implements the "Through" within a decade-wide bandwidth [24].

With a bandwidth of interest of 2 – 40 GHz, assumed in this experiment, the 1.20 cm- and 1.10 cm-long samples cover the bands of 2 – 20 GHz and 4 – 40 GHz, respectively. Therefore, this banded calibration enforces the samples' "band-to-band" measurement process. Finally, in performing the entire calibration process using the appropriate high-frequency VNA, as the ZVA 67 considered here, it is recommended to land the test ports' central pins in the middle of the samples' top conductor to limit errors.

Fig. 14 depicts the measured S_{11} and S_{22} at the two test ports after calibration while mounting a "Through" on the test fixture. For better readability, the banded results are merged into a single-band result. This simplification applies to all the results in this section.

Fig. 14 indicates that the reflection coefficient at the two test ports is smaller than −37.8 dB over the entire operating band of 2 – 40 GHz. This good matching level means that

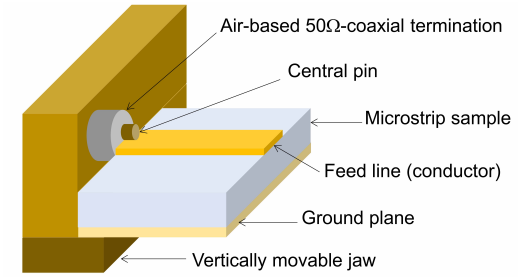

(a)

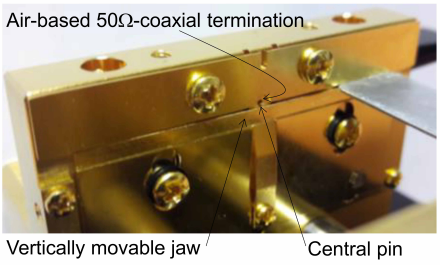

(b)

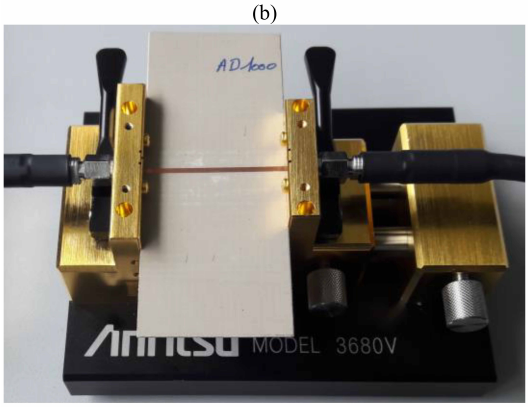

(c)

FIGURE 12. (a) : The general mounting set of a microstrip sample on a single test port, (b): zoom on a single test port, (c): photograph of the AD1000 sample mounted on the two-port RF test fixture.

(a)

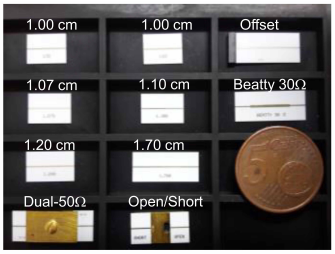

(b)

FIGURE 13. The microstrip calibration kit, (a): list of the available calibration samples and their properties, (b): photographs of the calibration samples.

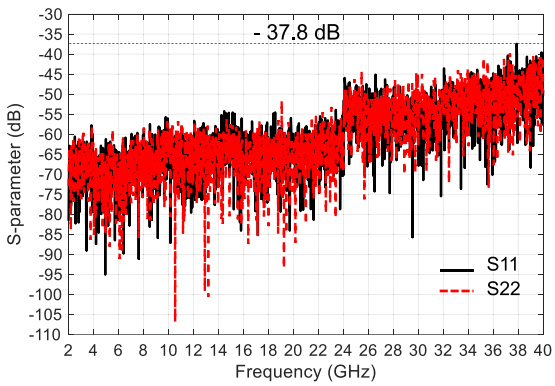

FIGURE 14. The measured reflection coefficients S_{11} and S_{22} at the two test ports after calibration, while mounting a "Through" on the test fixture. The calibration process is a band-to-band TRM two-port calibration whose results are merged into a single-band result for better readability. The initial calibration bands are 2 – 20 GHz and 4 – 40 GHz.

TABLE 4. Extracted and specified properties of the measured materials.

Materials	FR4 (2 GHz)		AD600L (10 GHz)		AD1000 (10 GHz)	
Properties	ε_r	$tan\delta$	ε_r	$tan\delta$	ε_r	$tan\delta$
Specified	4.2 ± 0.2	0.014 ± 0.002	6.15 ± 0.4	0.003	10.2 ± 0.35	0.0023
Extracted	4.4	0.0159	6.6	0.0027	10.5	0.0025
m value	0		1		1	

The phase mode value m is obtained from (8) for a start frequency at 2 GHz.

the calibration effectively compensates for the coaxial-to-microstrip transition effect, ensuring reliable measurements without parasitics.

D. RESULTS

Figs. 15a – 15c and 15d – 15f present the microstrip samples' measured reflection coefficients (S_{11}, S_{22}) and transmission coefficient S_{21}, respectively.

As expected, the FR4 sample is almost 50Ω-matched in the 2 – 20 GHz frequency band and starts to be mismatched above 20 GHz, creating little ripples on S_{21} due to surface wave effects. However, the AD600L and AD1000 are mismatched as expected, confirmed by ripples on S_{21} over the entire frequency band. Therefore, the correction in Fig. 4 applies to these two samples, as seen in Figs. 15e – 15f.

Applying the proposed approach to the measured samples provides the results in Figs. 15g – 15i and Fig. 15j for the extracted attenuation coefficient α and propagation constant β, respectively.

Figs. 15g – 15i indicates negligible conductor losses ($\alpha_{ce} \approx 0$) compared with dielectric losses in the three samples. This result fits the physics since the samples' metallization is copper, featuring a relatively high conductivity in the order of 10^7 S/m.

From the extracted dielectric loss $\alpha_{de} \approx \alpha$ in Figs. 15g–15i and the extracted propagation constant β in Fig. 15j, one can get the samples' permittivity ε_r and loss tangent $tan\delta$, as depicted in Figs. 15k and 15l, respectively.

The extracted properties (ε_r, $tan\delta$) correlate with the datasheets, as seen in Table 4, also providing the S_{21}-phase mode values from (8).

Regarding permittivity, the relative errors on FR4, AD600L, and AD1000 samples are 0.2, 0.45, and 0.3, which are close or equal to the datasheet tolerances of 0.2, 0.4, and 0.35, respectively. Moreover, the error on $tan\delta$ for the

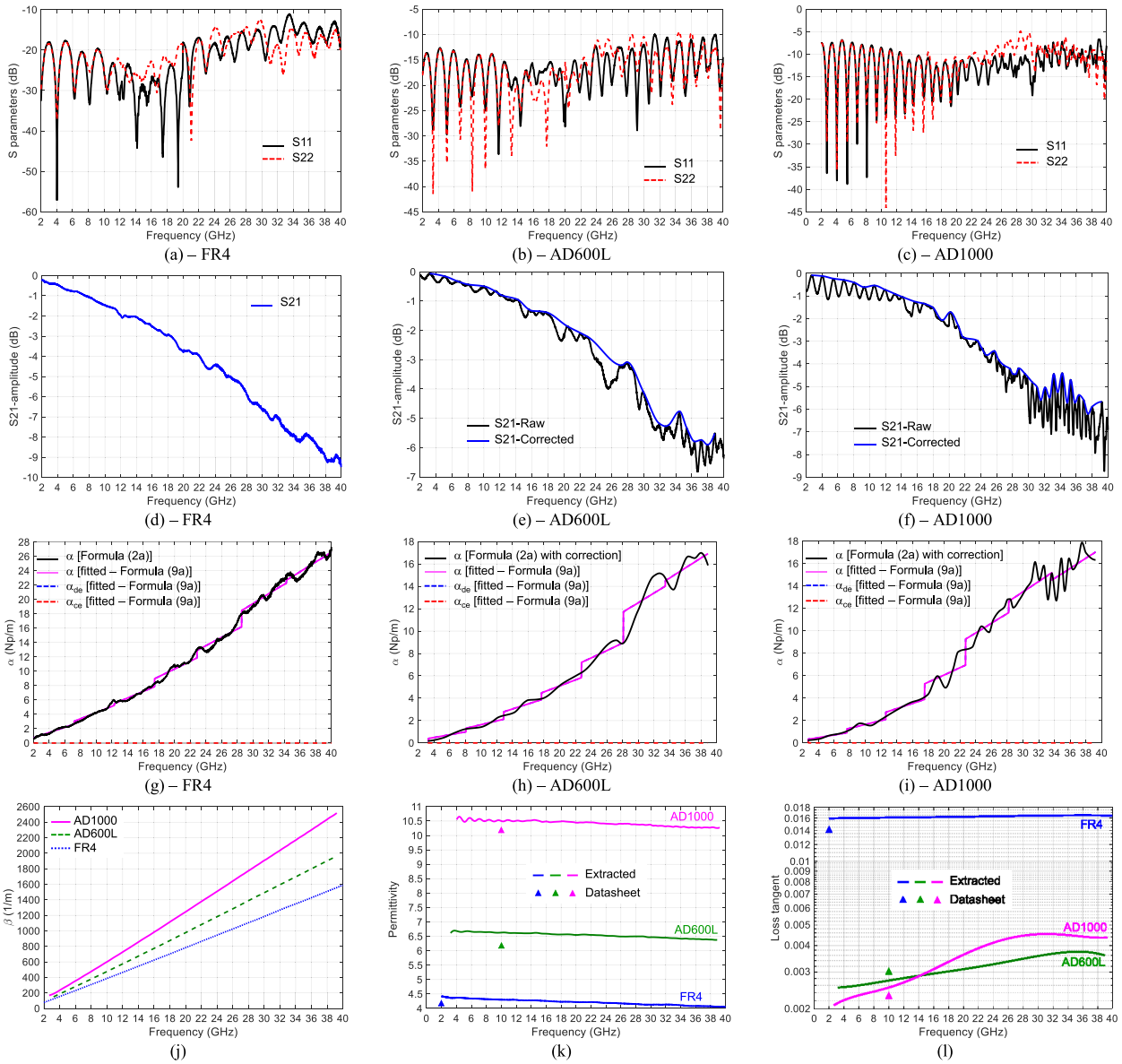

FIGURE 15. The measured properties of the fabricated microstrip samples, (a) – (c): reflection coefficients S_{11} and S_{22}, (d) – (f): transmission coefficient S_{21}, (g) – (i): extracted attenuation coefficient α, (j): extracted propagation constant β, (k): extracted permittivity ε_r, (l): extracted loss tangent $tan\delta$.

FR4 is 0.0019, near 0.002 claimed in the datasheet. The AD600L and AD1000 tolerances are not reported in their datasheets, but one can note minor errors of 0.0003 and 0.0002, respectively.

Beyond these slight error ranges on ε_r and $tan\delta$, the differences with the datasheets can be attributed to analytical errors and the samples' reduced length to $L = 40\ mm \approx 0.26\lambda$ (2 GHz), which is slightly smaller than the recommended length of $L \geq 0.3\lambda$ (Section IV-A). However, $L = 40\ mm$ is chosen as it almost fits the test fixture's size. Undoubtedly, longer samples will improve the results, which remain acceptable.

VI. CONCLUSION

This paper has dealt with a TO approach that solved the transmission phase ambiguity problem based on a linear frequency-dependent phase approximation. A unique propagation constant, suitable for low and wideband applications, has been derived based on the proposed phase mode analytical formula. The proposed approach was validated numerically and experimentally using microstrip samples. Validations included weakly and highly dispersive dielectrics with low and high losses.

REFERENCES

[1] A. M. Nicolson and G. F. Ross, "Measurement of the intrinsic properties of materials by time-domain techniques," *IEEE Trans. Instrum. Meas.*, vol. 19, no. 4, pp. 377–382, Nov. 1970.

[2] J. Baker-Jarvis, R. G. Geyer, and P. D. Domich, "A nonlinear least-squares solution with causality constraints applied to transmission line permittivity and permeability determination," *IEEE Trans. Instrum. Meas.*, vol. 41, no. 5, pp. 646–652, Oct. 1992.

[3] U. C. Hasar and C. R. Westgate, "A broadband and stable method for unique complex permittivity determination of low-loss materials," *IEEE Trans. Microw. Theory Techn.*, vol. 57, no. 2, pp. 471–477, Feb. 2009.
[4] W. B. Weir, "Automatic measurement of complex dielectric constant and permeability at microwave frequencies," *Proc. IEEE*, vol. 62, no. 1, pp. 33–36, Jan. 1974.
[5] M.-Q. Lee and S. Nam, "An accurate broadband measurement of substrate dielectric constant," *IEEE Microw. Guided Wave Lett.*, vol. 6, no. 4, pp. 168–170, Apr. 1996.
[6] M. Rodriguez-Vidal and E. Martin, "Contribution to numerical methods for calculation of complex dielectric permittivities," *Electron. Lett.*, vol. 6, no. 16, p. 510, 1970.
[7] O. Huber, T. Faseth, G. Magerl, and H. Arthaber, "Dielectric characterization of RF-Printed circuit Board materials by microstrip transmission lines and conductor-backed coplanar waveguides up to 110 GHz," *IEEE Trans. Microw. Theory Techn.*, vol. 66, no. 1, pp. 237–244, Jan. 2018.
[8] V. V. Varadan and R. Ro, "Unique retrieval of complex permittivity and permeability of dispersive materials from reflection and transmitted fields by enforcing causality," *IEEE Trans. Microw. Theory Techn.*, vol. 55, no. 10, pp. 2224–2230, Oct. 2007.
[9] M. Kirschning and R. H. Jansen, "Accurate model for effective dielectric constant of microstrip and validity up to millimeter-wave frequencies," *Electron. Lett.*, vol. 18, pp. 272–273, Mar. 1982.
[10] M. Kobayashi, "A dispersion formula satisfying recent requirements in Microstrip CAD," *IEEE Trans. Microw. Theory Techn.*, vol. 36, no. 8, pp. 1246–1250, Aug. 1988.
[11] W. J. Getsinger, "Microstrip dispersion model," *IEEE Trans. Microw. Theory Techn.*, vol. MTT-21, no. 1, pp. 34–39, Jan. 1973.
[12] A. K. Verma and R. Kumar, "A new dispersion model for microstrip line," *IEEE Trans. Microw. Theory Techn.*, vol. 46, no. 8, pp. 1183–1187, Aug. 1998.
[13] H. A. Wheeler, "Transmission-line properties of a strip on a dielectric sheet on a plane," *IEEE Trans. Microw. Theory Techn.*, vol. 25, no. 8, pp. 631–647, Aug. 1977.
[14] E. O. Hammerstad, "Equations for microstrip circuit design," in *Proc. 5th Eur. Microwave Conf.*, Hamburg, Germany, 1975, pp. 268–272.
[15] Z. Zhou and K. L. Melde, "A comprehensive technique to determine the broadband physically consistent material characteristics of microstrip lines," *IEEE Trans. Microw. Theory Techn.*, vol. 58, no. 1, pp. 185–194, Jan. 2010.
[16] M. A. C. Niamien, "Unique solution transmission-only approach for determination of dielectric properties of substrates," in *Proc. Internat. Conf. Electromag. Adv. Appl. (ICEAA)*, 2019, pp. 838–840.
[17] D. M. Pozar, *Microwave Engineering*, 4th ed. Hoboken, NJ, USA: Wiley, 2017.
[18] K. C. Gupta *et al.*, *Microstrip Lines and Slotlines*, 2nd ed., Norwood, MA, USA: Artech House, 1996.
[19] "Laird Microwave Absorbers." [Online]. Available: www.laird.com (Accessed: Jan. 2022).
[20] "CST Computer Simulation Technology." [Online]. Available: www.cst.com (Accessed: Jan. 2022).
[21] R. L. Weaver and Y.-H. Pao, "Dispersion relations for linear wave propagation in homogeneous and inhomogeneous media," *J. Math. Phys.*, vol. 22, pp. 1909–1918, Jun. 1981.
[22] "Bernier Electronik." [Online]. Available: https://bernierelectronik-boutique.fr/index.php (Accessed: Jan. 2022).
[23] "Rogers Corporation." [Online]. Available: www.rogerscorp.com (Accessed: Jan. 2022).
[24] "Anritsu." [Online]. Available: www.anritsu.com (Accessed: Jan. 2022).
[25] "Rohde & Schwarz." [Online]. Available: www.rohde-schwarz.com (Accessed: Jan. 2022).

CONSTANT M. A. NIAMIEN (Member, IEEE) received the M.Sc. and Ph.D. degrees in electrical engineering from the University of Rennes1, Rennes, France, in 2007 and 2010, respectively, and the "Habilitation à Diriger la Recherche" degree from the University of Rouen, France, in 2020.

He was with the Department of Antennas and Propagation, Centre of Nuclear Energy (CEA), Grenoble, France, as a Research Engineer in 2011. In addition, he was with LEMA, EPFL, Switzerland, as an Invited Researcher in 2010. In 2012, he joined EMITECH Group, Montigny-le-Bretonneux, France, as an Engineer. He joined ESIGELEC, IRSEEM, Normandie Univ, UNIROUEN, Rouen, France, as an Associate Professor in 2012. He has been a Full Professor with ESIGELEC since December 2020. He has coauthored French patent and mainly authored more than 50 journal and conference papers edited by IEEE and IET societies and Wiley periodicals. His research fields include multi-band and broadband antennas, antenna theory, electromagnetic modeling for antenna applications, receiving antennas, metasurfaces, rectennas for wireless ambient energy harvesting applications, and material characterization.

Prof. Niamien has been the project coordinator of four research projects (European, Regional) for overall attracted funding of more than €3.5 M. He has been a scientific contributor to three research projects. He has co-chaired two IEEE conference (APS, APMC) sessions. He has been a member of the European Association on Antennas and Propagation (EurAAP) since 2015 and a TPC Member of the "Journées Nationales Microondes" (JNM19) Caen, France.